Supporting information

Facile synthesis of MnO/NC nanohybrids toward high-efficiency ORR for zinc-air battery

Qingxi Zhuang,[§a] Chengjun Hu,[§a] Weiting Zhu,[a] Gao Cheng,*[a] Meijie Chen,[a] Ziyuan Wang,[b] Shijing Cai,[b] Litu Li,[a] Zier Jin,*[b] and Qiang Wang *[c]

[a] School of Chemical Engineering and Light Industry, Guangdong University of Technology, Guangzhou 510006, China.

[b] Foshan Institute of Environment and Energy Technology, Foshan 528000, China.

[c] School of Materials and Energy, Chongqing Key Laboratory for Advanced Materials and Technologies of Clean Energies, Southwest University, Chongqing 400715, China.

[§] These authors contributed equally to this work.

[*] Corresponding author.

E-mail address: chengg36@gdut.edu.cn; fieet0325@163.com; wysnu@swu.edu.cn

Experimental

Characterizations

The crystal structures of products were analyzed by X-ray diffraction (XRD, Aeris), utilizing Cu-Kα radiation with an applied voltage of 15 kV and an electrical current of 40 mA, across a 2θ range of 10~80°. Raman spectra were recorded using a 532-nanometre laser on a Raman spectrometer (LabRAM HR Evolution). The morphologies and microstructures of as-prepared samples were studied by field emission scanning electron microscopy (FESEM, SU8220) at a 15 kV accelerating voltage and field emission scanning electron microscopy (FETEM, Tecnai G2F30) at a 300 kV accelerating voltage. The elemental compositions and their contents and surface bonding states were characterized by X-ray photoelectron spectroscopy (XPS, Escalab 250 XI). The monochromatic radiation energy of Al Kα was set at 1486.6 eV. The measured spectrum was corrected for the amorphous carbon peak (C 1s) at 284.8 eV.

Electrochemical measurements

Electrochemical measurements were performed using a CHI 760E electrochemical workstation equipped with a standard three-electrode electrochemical cell. Rotating disk electrode (RDE)/rotating ring disk electrode (RRDE), Ag/AgCl electrode (3.5 M KCl), and graphite rod were used as working electrode, reference electrode, and counter electrode, respectively. The catalyst ink was prepared as follows: 7.5 mg of catalyst was added to a solution containing 950 μL ethanol and 50 μL Nafion, and the mixed solution was then treated by sonication for 1 h. The homogeneous ink was dropped onto the RDE/RRDE for electrochemical tests. The mass loading on the RDE/RRDE was ~ 0.27 mg cm^{-2}. All potentials in this study were converted to reversible hydrogen electrode (RHE) using the equation: $E_{RHE} = E_{Ag/AgCl} + 0.059 \times pH + 0.2046$, where $E_{\mathrm{Ag/AgCl}}$ is the measured potential vs. Ag/AgCl electrode. Cyclic voltammetry (CV) was performed in O_2-saturated 0.1 M KOH at a scan rate of 50 mV/s. And linear sweep voltammetry (LSV) was tested in

O_2-saturated 0.1 M KOH at a scan rate of 5 mV/s.

For the Tafel slope, kinetic current density (J_K) is corrected through the diffusion current density (J_L) from the Koutecky-Levich (K-L) equation (1):

$$J_K = \frac{J_L \times J}{J_L - J} \quad (1)$$

K-L plots (J^{-1} vs. $\omega^{-1/2}$) are obtained at different potentials and fitted to linear curves using the following K-L equation (2) to calculate the number of electrons transferred (n):

$$\frac{1}{J} = \frac{1}{J_L} + \frac{1}{J_k} = \frac{1}{B\omega^{1/2}} + \frac{1}{J_k} \quad (2)$$

where ω is the rotating rate. B is determined from the slope of K-L plots based on equation (3):

$$B = 0.62nFC_0(D_0)^{2/3}v^{-1/6} \quad (3)$$

where F is the Faraday constant (96485 C mol^{-1}), n is the number of electrons transferred per molecule of oxygen, C_0 is the bulk concentration of O_2 (1.2×10^{-6} mol cm^{-3}), D_0 is the diffusion of diffusion of O_2 (1.9×10^{-5} cm^2 s^{-1}), and v is the kinetic viscosity of the electrolyte (0.01 cm^2 s^{-1})

Electron transfer number (n) and H_2O_2 yield were tested using RRDE and calculated using the following equations (4) and (5):

$$H_2O_2\, yield = 200 \times \frac{J_R/N}{J_D + J_R/N} \quad (4)$$

$$n = \frac{4 \times J_D}{J_D + J_R/N} \quad (5)$$

where J_D and J_R are the disc and ring current densities, respectively, and N (0.37, using $[Fe(CN)]^{3-}$/$[Fe(CN)_6]^{4-}$ redox couple) is the collection efficiency of Pt ring.

Double-layer capacitance (C_{dl}) was calculated from cyclic voltammetry at different scan rates in the non-Faradic region (1.07~1.22 V). C_{dl} value is derived from the following equation (6):

$$C_{dl} = \frac{|j_a - j_c|}{2d(v_b)} \quad (6)$$

v_b = scan rate variance, j_a - j_c = the change in current density.

ECSA value is derived from the following equation (7):

$$ECSA = \frac{C_{dl}}{C_s} \quad (7)$$

C_s is the specific capacitance of the as-synthesized sample.

Aqueous Zinc-air battery assembly and test

The aqueous ZAB performance was measured on an electrochemical workstation (CHI 760E) and a battery testing system (LAND, CT3001A 1U). The dried catalyst with a loading of ~ 1.00 mg cm^{-2} was uniformly coated on the stainless steel mesh as an air electrode. A polished zinc plate was used as the negative electrode, and the electrolyte consisted of KOH (6 M) and $Zn(CH_3COO)_2$ (0.2 M).

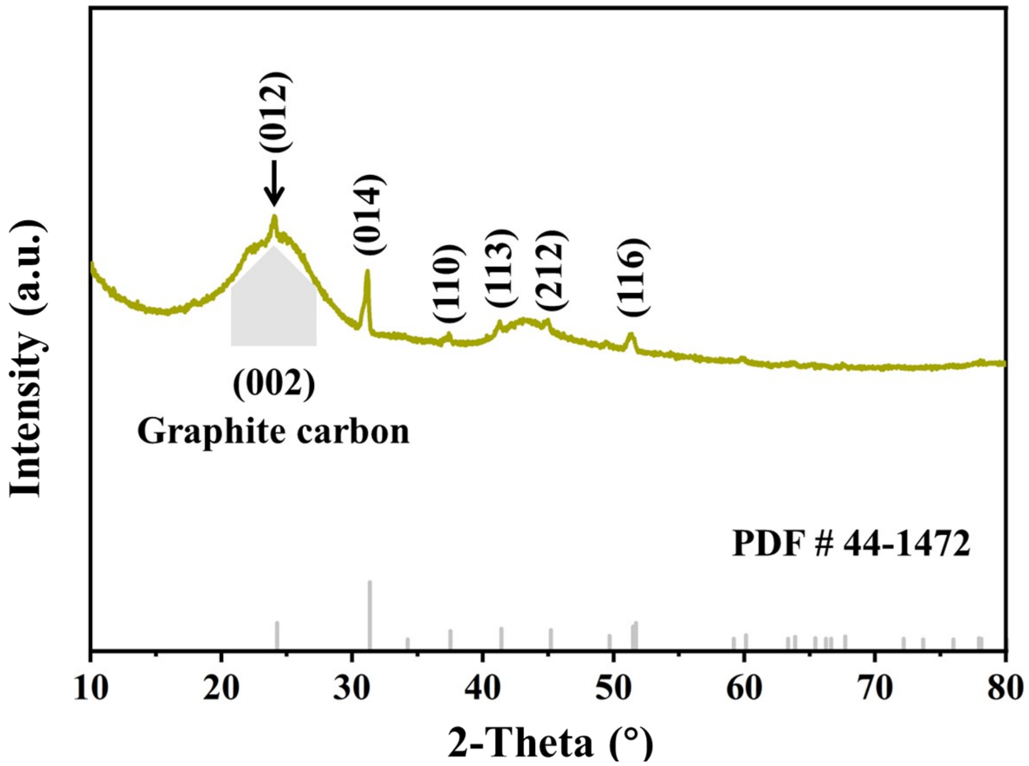

Fig. S1 XRD image of $MnCO_3$/NC.

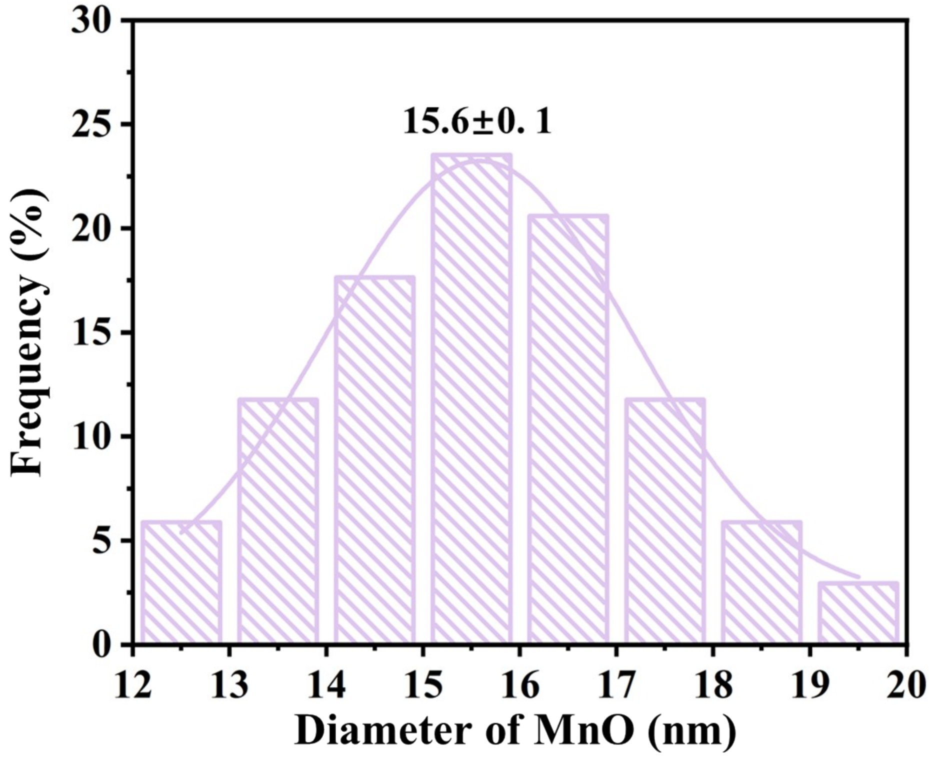

Fig. S2 Particle-size distribution of MnO nanoparticles on the MnO/NC-900.

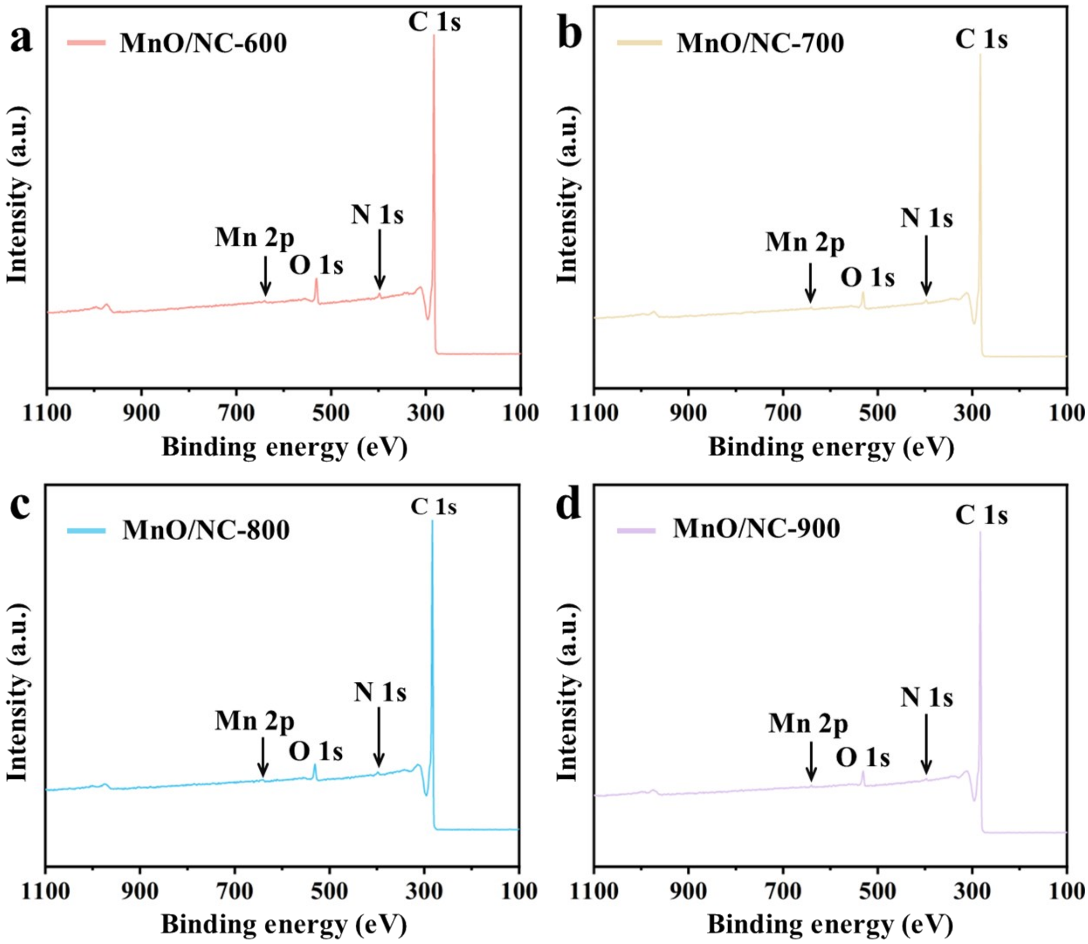

Fig. S3 XPS survey spectra of (a) MnO/NC-600, (b) MnO/NC-700, (c) MnO/NC-800, and (d) MnO/NC-900.

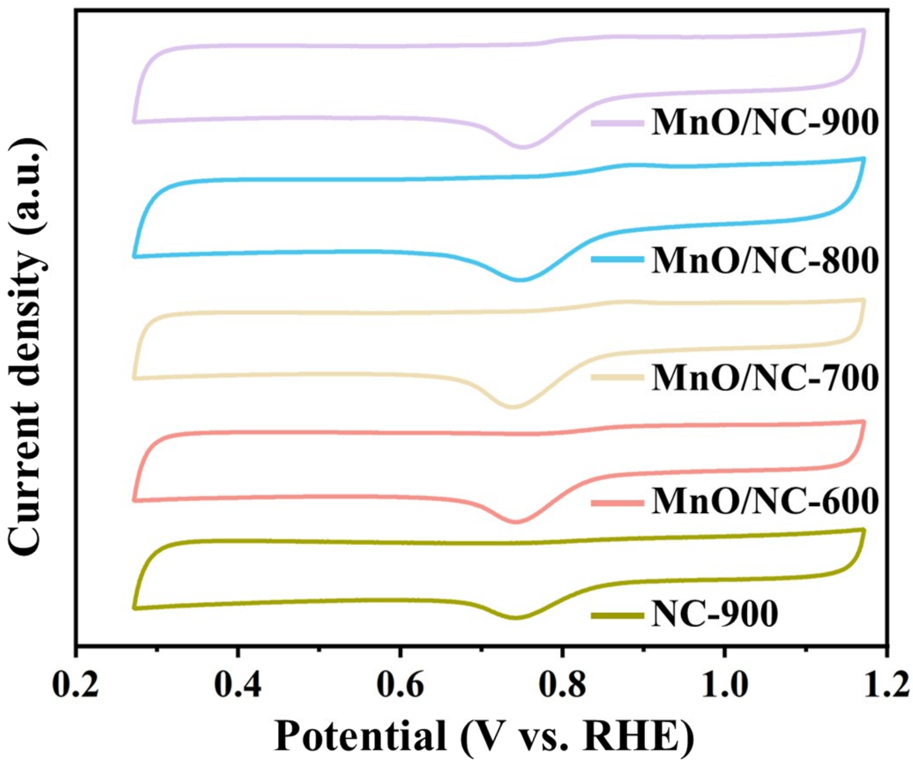

Fig. S4 CV curves of MnO/NC-600, MnO/NC-700, MnO/NC-800, MnO/NC-900, and NC-900 in O_2-saturated 0.1 M KOH electrolyte at a scan rate of 50 mV s^{-1}.

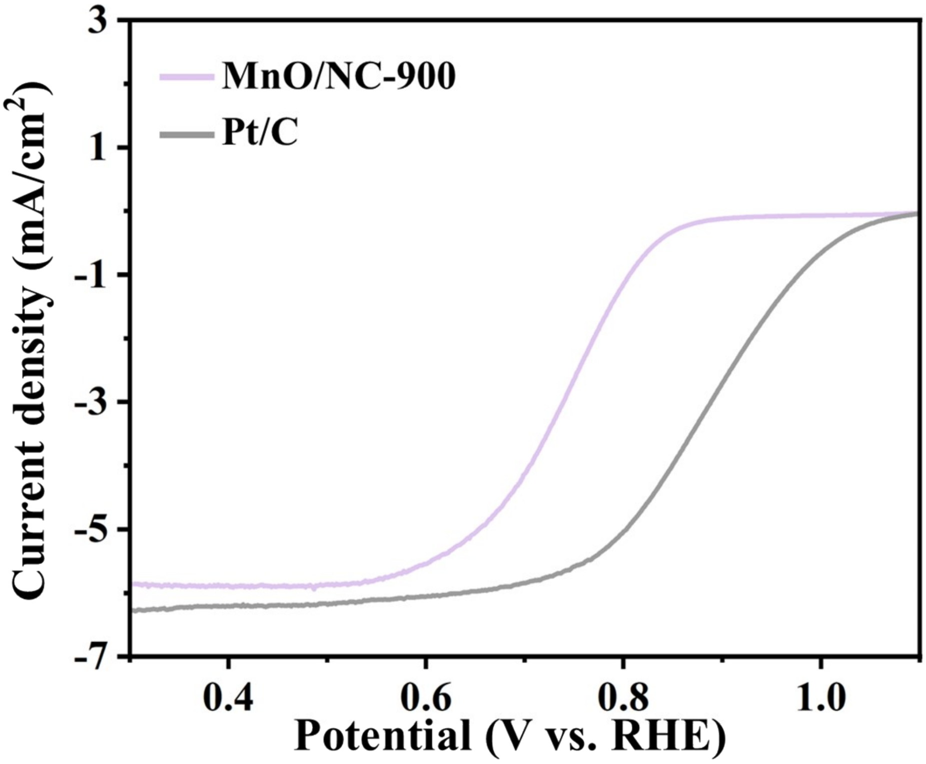

Fig. S5 LSV curves of MnO/NC-900 and Pt/C at 1600 rpm.

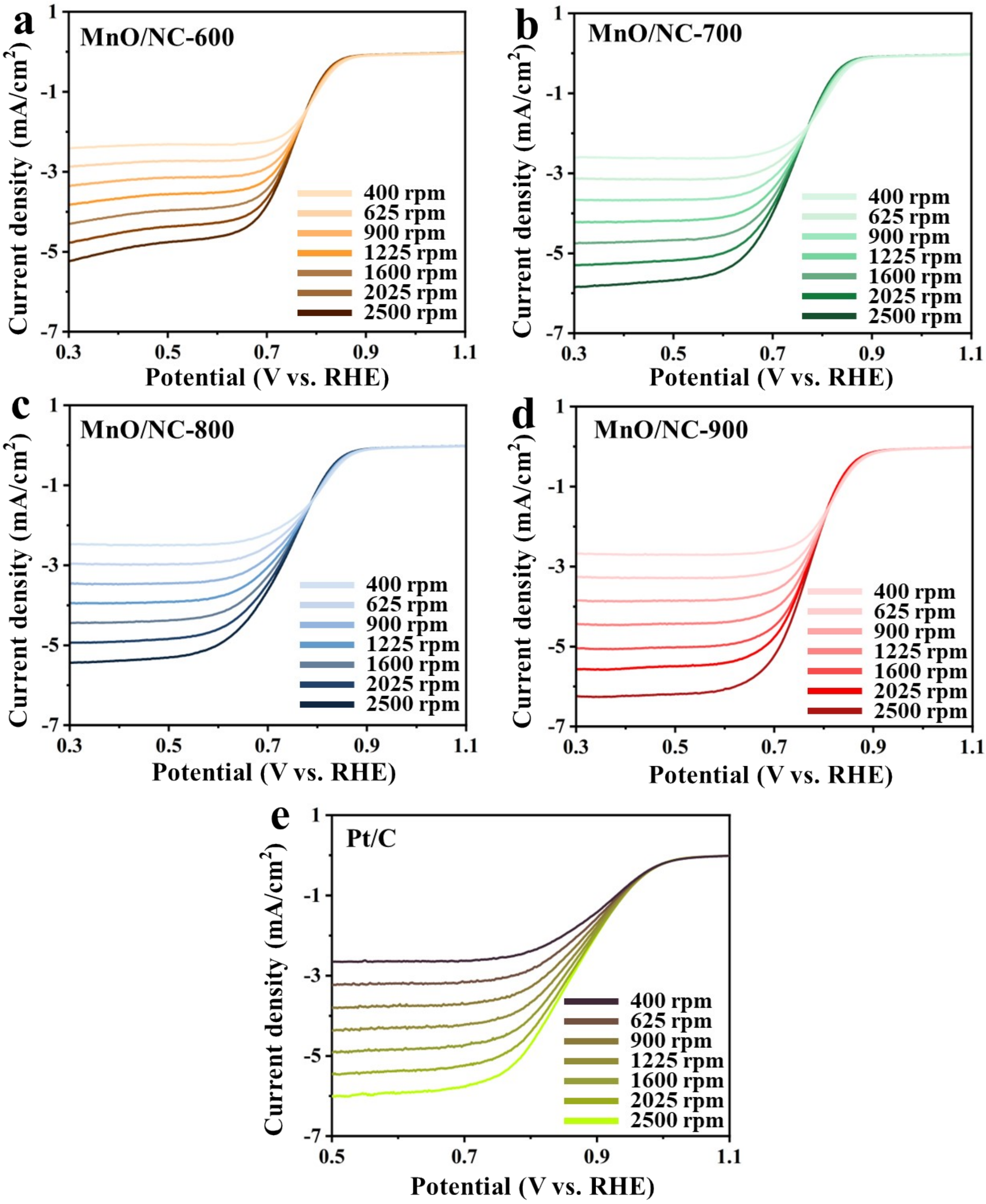

Fig. S6 LSV curves of (a) MnO/NC-600, (b) MnO/NC-700, (c) MnO/NC-800, (d) MnO/NC-900, and (e) Pt/C with different rotation rates.

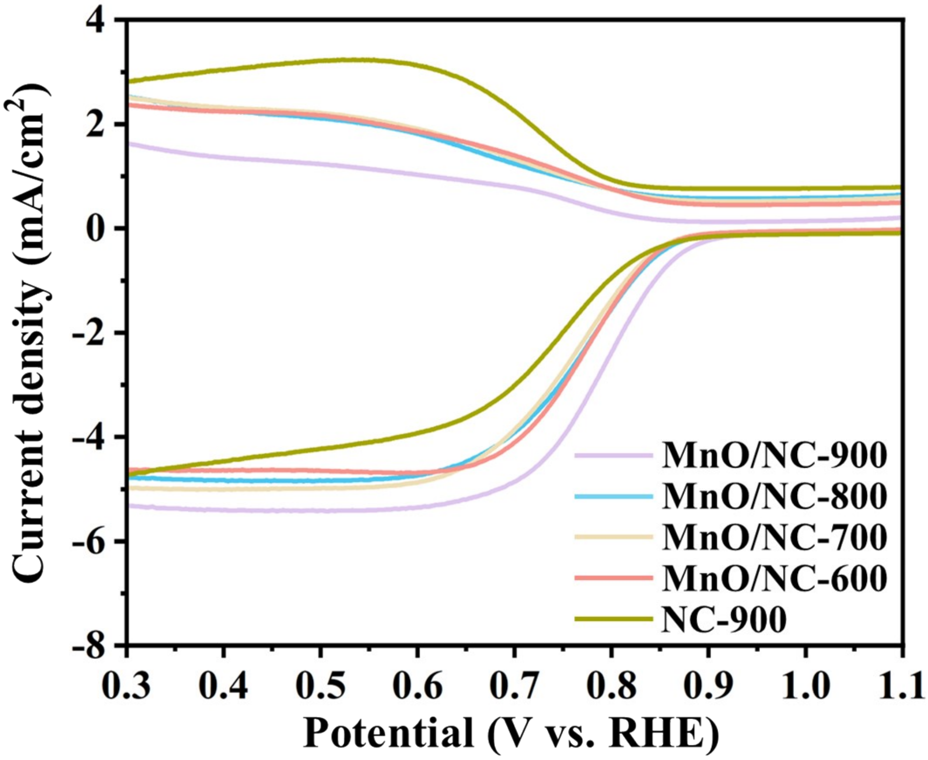

Fig. S7 RRDE polarization curves of MnO/NC-600, MnO/NC-700, MnO/NC-800, MnO/NC-900, and NC-900 in O_2-saturated 0.1 M KOH solution at a rotation rate of 1600 rpm.

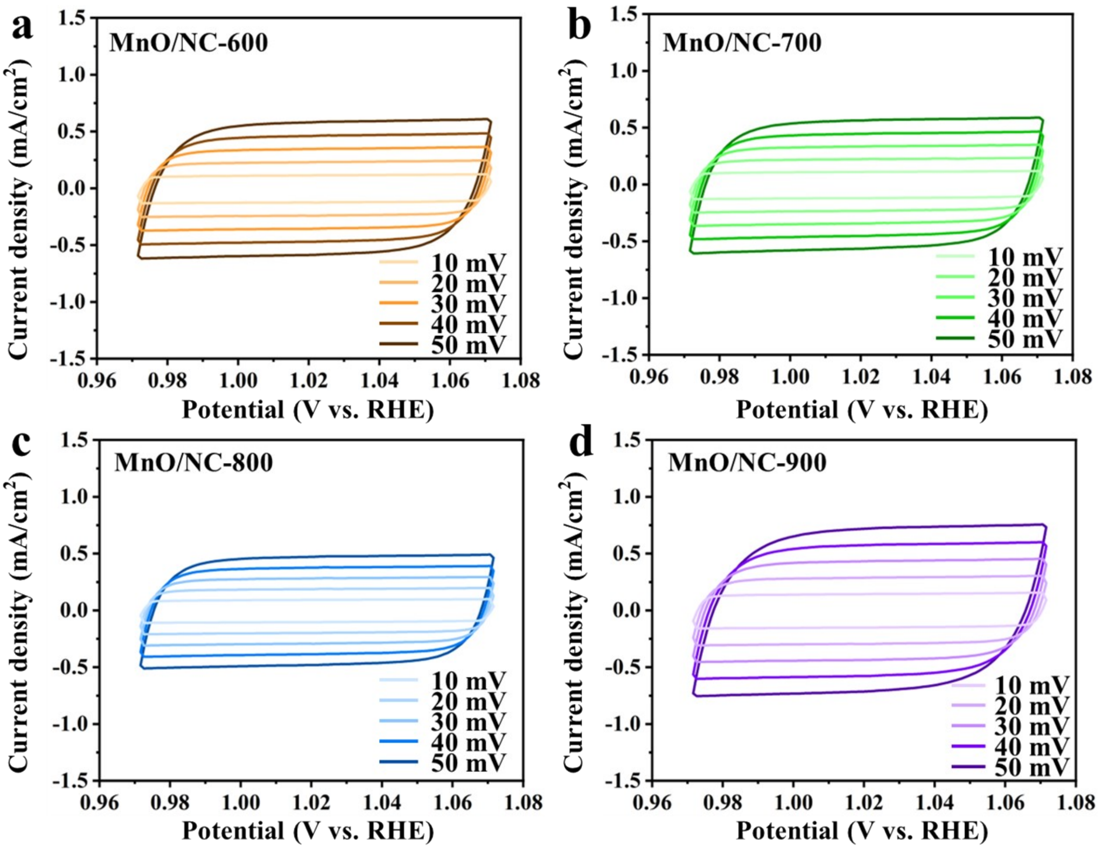

Fig. S8 CV curves for ORR at various scan rates: (a) MnO/NC-600, (b) MnO/NC-700, (c) MnO/NC-800, and (d) MnO/NC-900.

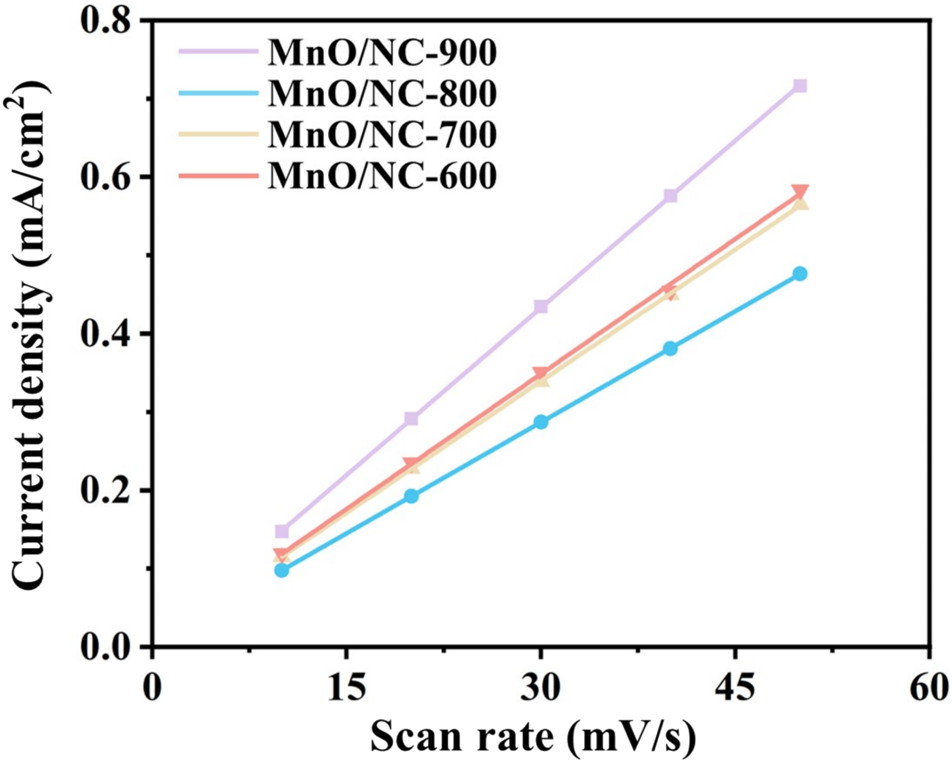

Fig. S9 Current density to scanning rate of MnO/NC-600, MnO/NC-700, MnO/NC-800, and MnO/NC-900.

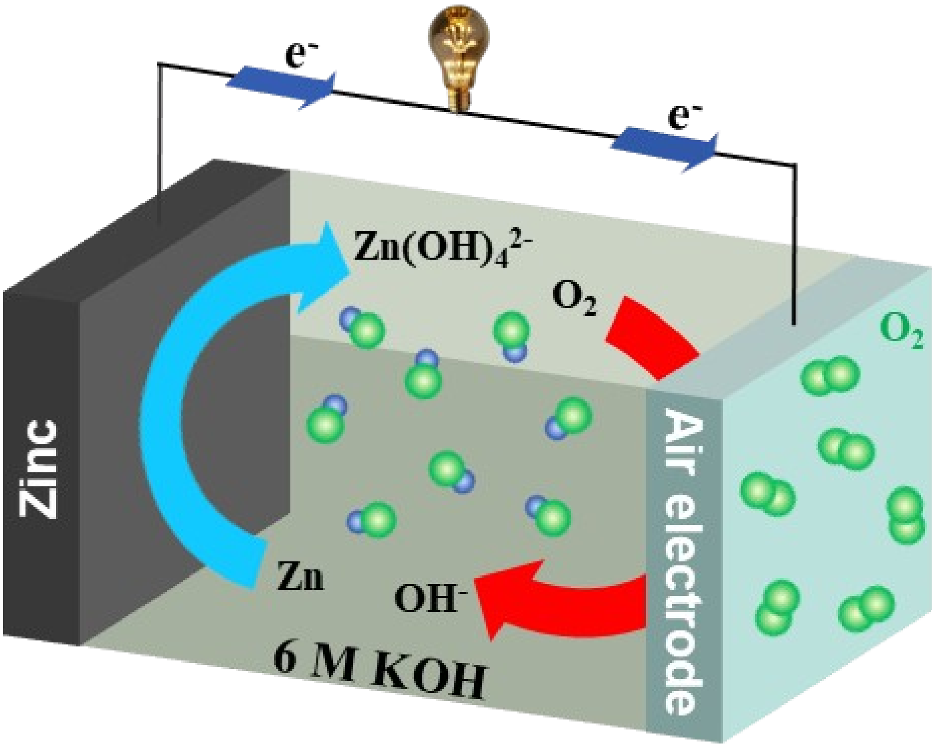

Fig. S10 A schematic showing the aqueous ZAB configuration.

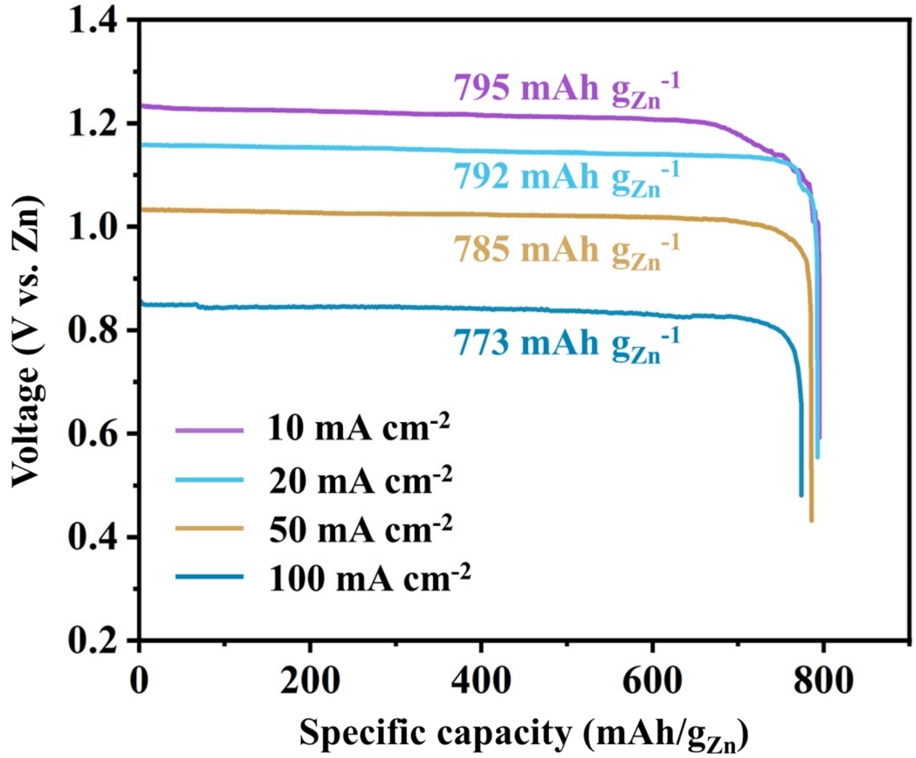

Fig. S11 Discharge curves of MnO/NC-900-ZAB till complete Zn consumption at diverse current densities.

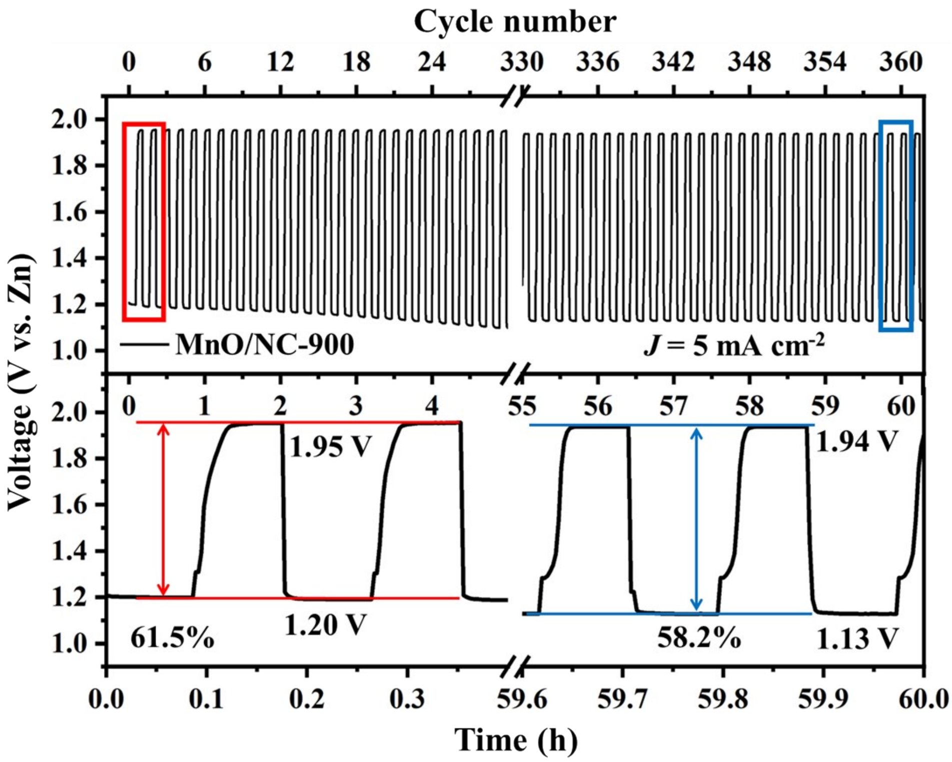

Fig. S12 Galvanostatic charge-discharge cycling performance and corresponding voltage efficiency based on MnO/NC-900-ZAB at a current density of 5 mA cm^{-2}.

Sample	Mn	C	N	O
MnO/NC-600	0.11	95.0	1.11	3.78
MnO/NC-700	0.06	96.2	0.76	2.98
MnO/NC-800	0.11	96.5	0.61	2.78
MnO/NC-900	0.08	96.9	0.19	2.83

Table S1. Element contents in the MnO/NC samples measured by XPS.

Table S2. Relative proportions of pyridinic-N, pyrrolic-N, graphitic-N, and oxidized-N in the MnO/NC samples measured by XPS.

Sample	pyridinic-N	pyrrolic-N	graphitic-N	oxidized-N
MnO/NC-600	30.5	44.4	9.40	15.7
MnO/NC-700	32.7	41.2	13.2	12.9
MnO/NC-800	35.0	35.8	13.9	15.3
MnO/NC-900	37.2	30.1	18.7	14.0

Table S3. Relative proportions of O_α, O_β, and O_γ in the MnO/NC samples measured by XPS.

Sample	O_α	O_β	O_γ
MnO/NC-600	43.2	38.2	18.6
MnO/NC-700	35.9	47.6	16.5
MnO/NC-800	39.8	48.2	12.0
MnO/NC-900	34.7	49.0	16.3

Table S4. The ORR performance of reported Mn-based catalysts for comparison.

Catalysts	$E_{1/2}$ **(V vs. RHE)**	**References**
MnO/NC-900	0.74	This work
MnO/RGO	0.60	1
MnO@CNT	0.70	2
MnO/N-CC-2	0.69	3
MnO/CC	0.72	4
MnO@NC-1100	0.74	5
N-CN@MnO	0.69	6
MnO	0.63	7
NC/MnO_2/NC (15)	0.73	8
Mn-defected Mn_3O_4	0.65	9
H-β-MnO_2	0.69	10
Mn_2O_3 nanoballs	0.68	11
γ-MnO_2	0.66	12
MnO_2 nanoflakes	0.67	13
Cu-α-MnO_2 nanowires	0.71	14
λ-MnO_2-Z	0.67	15

References

1 Q. L. Wu, M. L. Jiang, X. F. Zhang, J. N. Cai and S. Lin, A novel octahedral MnO/RGO composite prepared by thermal decomposition as a noble-metal free electrocatalyst for ORR, *J. Mater. Sci.*, 2017, **52**, 6656-6669.

2 F. Li, T. T. Qin, Y. P. Sun, R. J. Jiang, J. F. Yuan, X. Q. Liu and A. P. O'Mullane, Preparation of a one-dimensional hierarchical MnO@CNT@Co-N/C ternary nanostructure as a high-performance bifunctional electrocatalyst for rechargeable Zn-air batteries, *J. Mater. Chem. A*, 2021, **9**, 22533-22543.

3 W. Hao, S-H. Lee and S. G. Peera, Xerogel-derived manganese oxide/N-doped carbon as a non-precious metal-based oxygen reduction reaction catalyst in microbialfuel cells for energy conversion applications, *Nanomaterials*, 2023, **13**, 2949.

4 Q. Liu, P. Z. Qiao, M. M. Tong, Y. Xie, X. X. Zhang, K. Lin, Z. J. Liang, L. Wang and H. G. Fu, Enhancing zinc-air battery performance by constructing three-dimensional N-doped carbon coating multiple valence Co and MnO heterostructures *Nano Res.*, 2024, **17**, 5104-5113.

5 L-Q. Ji, J. Yang, Z-Y. Zhang, Y. Qian, Z. Su, M. Han and H-K. Liu, Enhanced catalytic performance for oxygen reduction reaction erived from nitrogen-richtetrazolate-based heterometallic metal-organic frameworks, *Cryst Growth Des*, 2019, **19**, 2991-2999.

6 M. G. Wang, F. Peng, M. Wang and J. Han, N-doped carbon nanospheres with nanocavities to encapsulate manganese oxides as ORR electrocatalysts, *New J. Chem.*, 2022, **44**, 14915-14921.

7 K. X. Lei, X. P. Han, Y. X. Hu, X. Liu, L. Cong, F. Y. Cheng and J. Chen, Chemical etching of manganese oxides for electrocatalytic oxygen reduction reaction, *Chem. Comm.,* 2015, **51**,11599-11602.

8 Y. N. Li, S. Y. Cao, L. Fan, J. Han, M. G. Wang and R. Guo, Hybrid shells of MnO_2 nanosheets encapsulated by N-doped carbon towards nonprecious oxygen reduction reaction catalysts, *J. Colloid Interface Sci.*, 2018, **527**, 241-250.

9 Y-C. Zhang, S. Ullah, R. R. Zhang, L. Pan, X.W Zhang and J-J. Zoua, Manipulating electronic delocalization of Mn_3O_4 by manganese defects for oxygen reduction reaction, *Appl Catal B-Environ*, 2020, **277**, 119247.

10 G. Cheng, P. Liu, S. H. Chen, Y. X. Wu, L. H. Huang, M. J. Chen, C. J. Hu, B. Lan, X. H. Su, M. Sun, and L. Yu, Self-templated formation of hierarchical hollow β-MnO_2 microspheres with enhanced oxygen reduction activities, *Colloid Surface A*, 2022, **637**, 128228.

11 S. Ghosh, P. Kar, N. Bhandary, S. Basu, S. Sardar, T. Maiyalagan, D. Majumdar, S. K. Bhattacharya, A. Bhaumik, P. Lemmens and S. K. Pal, Microwave-assisted synthesis of porous Mn_2O_3 nanoballs as bifunctional electrocatalyst for oxygen reduction and evolution reaction, *Catal. Sci. Technol.*, 2016, **6**, 1417-1429.

12 B. Zhang, G. Cheng, B. Lan, X. Zheng, M. Sun, F. Ye, L. Yu and X. Cheng, Crystallization design of MnO_2 via acid towards better oxygen reduction activity, *CrystEngComm,* 2016, **18**, 6895-6902.

13 C. Wei, L. Yu, C. Cui, J. Lin, C. Wei, N. Mathews, F. Huo, T. Sritharan and Z. Xu, Ultrathin MnO_2 nanoflakes as efficient catalysts for oxygen reduction reaction, *Chem. Commun.*, 2014, **50**, 7885-7888.

14 D. J. Davis, T. N. Lambert, J. A. Vigil, M. A. Rodriguez, M. T. Brumbach, E. N. Coker and S. J. Limmer, Role of Cu-ion doping in Cu-α-MnO_2 nanowire electrocatalysts for the oxygen reduction reaction, *J. Phys. Chem. C*, 2014, **118**, 17342-17350.

15 S. Lee, G. Nam, J. Sun, J.-S. Lee, H.-W. Lee, W. Chen, J. Cho and Y. Cui, Enhanced intrinsic catalytic activity of λ-MnO_2 by electrochemical tuning and oxygen vacancy generation, *Angew. Chem. Int. Ed.,* 2016, **55**, 8599-8604.